

Spherical harmonics method for computing the image stress due to a spherical void

Yifan Wang, Xiaohan Zhang, Wei Cai

Department of Mechanical Engineering, Stanford University, CA 94305-4040, USA

Abstract

We develop an efficient numerical method for calculating the image stress field induced by spherical voids in materials, and applied the method to dislocation-void interactions. The method is constructed based on a complete set of basis functions for the displacement potential of the elastic boundary value problem for a spherical hole, as well as the corresponding displacement, stress, and traction fields, all in terms of linear combinations of spherical harmonics. Using the fast transformation between the real and spherical-harmonics spaces provided by the SHTOOLS package, the method is more efficient than other image stress solvers such as the finite-element method. This method can be readily extended for solving elasticity problems involving inclusions and inhomogeneities, as well as contact between spheres. The tools developed here can also be useful for fast solution of differential equations with spherical boundaries beyond elasticity.

Keywords: image stress, void, dislocation, spherical harmonics

1. Introduction

Fracture of ductile materials is mainly controlled by the nucleation, growth and coalescence of the voids in the material (Tvergaard, 1989). In continuum models, the growth of micro-voids ($>10\ \mu\text{m}$) can be described by the plastic flow of the material around a spherical hole (Benzerga et al., 2016). For very small voids ($<100\ \text{nm}$), such as during the initial state of void growth, the kinetics is controlled by dislocation loop emitting from the void (i.e. material being punched out from the void) (Lubarda et al., 2004). This dislocation loop emission mechanism has been studied by atomistic simulations (Traiviratana et al., 2008; Potirniche et al., 2006a, 2006b). However, for the

intermediate-size voids ($\sim 1 \mu\text{m}$), the growth kinetics is too large for atomistic models and too small to be adequately described by continuum models. The growth kinetics of micron-sized voids is influenced by not only the dislocations emitting from the void surface, but also the nearby dislocations interacting with the void surface (Chang et al., 2015), which usually happens in the length scale of $1 \mu\text{m}$ to $10 \mu\text{m}$, greatly exceeding the length scale of atomistic simulations. At this intermediate length-scale, dislocation dynamics (DD) simulation becomes a suitable tool to study the growth kinetics of voids.

DD simulation is a method to quantitatively link the macroscopic plasticity of crystalline materials with the underlying dislocation structures and interactions (Arsenlis et al., 2007). Under a wide range of temperature and strain rate conditions, plastic deformation is dominated by dislocation motion and interactions. By considering only the dislocation lines instead of keeping track of all the atomic positions, DD simulations can reach a length scale of $\sim 10 \mu\text{m}$ at a time scale of $1 \mu\text{s}$ (Sills et al., 2016), which is comparable to the scale of interest for micron-sized void growth kinetics. This means that potentially, it is possible to model *all* the dynamical behavior of dislocations around the void, the void-dislocation interactions, and their influence to the void growth kinetics, hence filling the gap between the atomistic modeling of the very small voids and the continuous modeling of the large voids.

Over the last ten years, DD simulations have been used to understand the size effect of void-dislocation interactions in two dimensions (Segurado and Llorca, 2009, 2010) and in three dimensions (Munday et al., 2015). However, all these works have been limited to small strain and low dislocation density. In these works, the finite-element method (FEM) has been used for solving the image stress needed to satisfy the boundary condition associated with the interaction between dislocations and the free surface of the void. Since the image stress needs to be solved at every iteration of the DD simulation, the accuracy and efficiency of DD simulations for void-growth problems have been limited by the FEM image stress solver.

In this work, we develop a semi-analytical image stress solver for spherical interfaces. Our method provides a good description of dislocation-void interactions when the void shape remains spherical. This is expected to be the case when the surface steps produced by dislocations intersecting the void are much smaller than the void dimension and when the stress triaxiality is sufficiently high, where diffusion is rapid enough so that the void can maintain its spherical shape while growing in volume. We find a complete set of

basis functions for the solution of elasticity problem represented in terms of linear combination of spherical harmonic functions. With the help of the fast spherical harmonic transformation provided by SHTOOLS (Wieczorek et al., 2016), our method finds a superposition of the basis functions that satisfies an arbitrary traction boundary condition on a spherical interface. Because finding the correct superposition to satisfy the boundary condition requires only the solution of a sparse linear system on the spherical surface, this method has higher accuracy and efficiency compared with other solvers such as FEM and 3D-FFT (Lebensohn et al., 2013), which require 3D meshing of the material volume, and the boundary element method (BEM), which requires the solution of a dense linear system. The method relies on the availability of the coefficients of the basis functions and their displacement, stress and traction fields in terms of the spherical harmonic expansion. These coefficients are pre-computed using ShElastic toolbox developed in this work, which is built on top of a set of symbolic manipulation tools (specifically multiplication and spatial derivatives) for functions expressed in the spherical harmonics space. These symbolic tools are likely to be useful for solving other partial differential equations with spherical boundaries beyond elasticity.

This paper is organized as follows: In section 2, we formulate the image stress problem using the dislocation-void interaction as an example. In section 3, we develop the spherical harmonic solution for the image stress problem. In section 4, we present numerical results of several classical elasticity problems, including the dislocation-void interaction, to validate the method. Discussions on further generalizations of the method are given in section 5. The appendices provide derivations needed for the development of the ShElastic toolbox.

2. Image stress problem

In DD simulations, the dislocation lines are discretized into straight segments connecting a set of nodes, which are the degrees of freedom (DOF) in the model (Arsenlis et al., 2007). In every time step of DD simulation, the most time consuming stage is evaluating the forces acting on the nodes. The Peach-Koehler force per unit length acting on the dislocation segment is calculated as:

$$\mathbf{f} = (\boldsymbol{\sigma}^{\text{tot}} \cdot \mathbf{b}) \times \boldsymbol{\xi} \quad (1)$$

where \mathbf{b} is the Burger's vector, and ξ is the line direction vector. $\boldsymbol{\sigma}^{\text{tot}}$ is the total stress field acting on the dislocation segment. When the solid has a spherical (internal) surface $\partial\Omega$ that satisfies the traction-free boundary condition, the total stress field $\boldsymbol{\sigma}^{\text{tot}}$ can be obtained as the superposition of two fields $\boldsymbol{\sigma}^\infty$ and $\boldsymbol{\sigma}^{\text{img}}$ (van der Giessen and Needleman, 1995), which are the solutions of two subproblems, as shown in figure 1 (a) and (b), respectively.

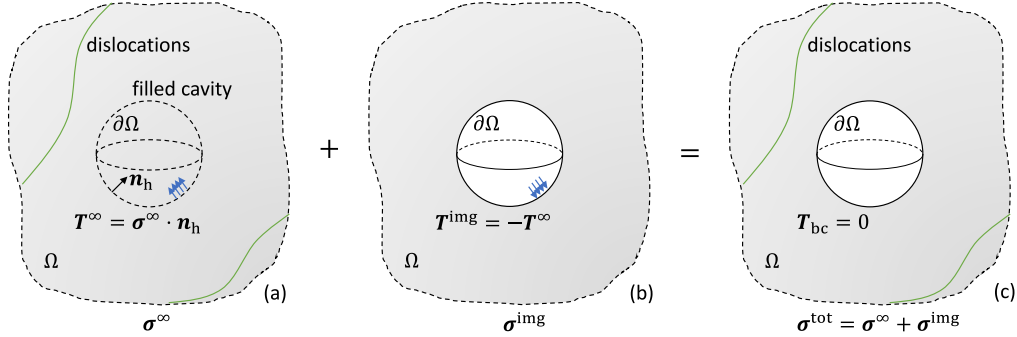


Figure 1: Decomposition of the stress field in DD simulation. (a) Dislocations in an infinite medium without the spherical boundary $\partial\Omega$. (b) The image stress problem: an infinite medium containing the void with traction \mathbf{T}^{img} on the void surface. (c) The original problem: an infinite medium containing dislocations and the void with zero traction on the void surface $\partial\Omega$ as a superposition of (a) and (b).

Let the stress induced by all the dislocations and external applied stress in an infinite elastic continuum (with no boundaries) be $\boldsymbol{\sigma}^\infty$, as shown in figure 1(a), and let the corresponding displacement field be \mathbf{u}^∞ . Both $\boldsymbol{\sigma}^\infty$ and \mathbf{u}^∞ of a given dislocation structure in an infinite medium can be obtained analytically (Hirth and Lothe, 1982; Cai et al., 2006). A traction field \mathbf{T}^∞ on the spherical boundary $\partial\Omega$ is required if $\boldsymbol{\sigma}^\infty$ is applied to the domain Ω , where $\mathbf{T}^\infty = \boldsymbol{\sigma}^\infty \cdot \mathbf{n}_h$ and \mathbf{n}_h is the surface normal of the hole (i.e. \mathbf{n}_h points towards the center of the sphere). To satisfy the traction-free boundary condition in the original problem shown in figure 1 (c), an image traction $\mathbf{T}^{\text{img}} = -\mathbf{T}^\infty$ is introduced to cancel the \mathbf{T}^∞ on the spherical surface $\partial\Omega$. The stress field in the continuum Ω induced by the image-traction boundary condition is called the image stress $\boldsymbol{\sigma}^{\text{img}}$. Here the *image stress problem* refers to the boundary-value problem on a spherical surface for solving $\boldsymbol{\sigma}^{\text{img}}$ as shown in figure 1(b). The detailed definition of the boundary value problems of the three problems can be found in Appendix D.

For certain boundary shapes, it is possible to use the symmetries of the

geometry to derive semi-analytical solutions to reach both high efficiency and accuracy, such as Weinberger and Cai (2007), who developed a general method for solving the image stress problem on a cylindrical shape boundary based on fast Fourier transform (FFT). For spherical-shaped boundaries, analytical solutions have only been developed for a number of specific problems. For example, Willis et al. (1972) and Gavazza and Barnett (1974) developed analytical solutions for the interaction between an infinite straight screw dislocation and a spherical void; and Sadraie et al. (2007) developed analytical solutions for the interaction between inclusions and cavities. For the void-growth problem which requires DD simulations with voids, it is of interest to develop a general image stress solver for spherical voids subjected to arbitrary image tractions (produced by curved dislocation lines) with higher accuracy and efficiency than other general methods for elasticity such as FEM.

In this paper, we develop such a semi-analytical method, which solves the image stress problem with any arbitrary traction on the boundary of a spherical hole in an infinite medium. Using this method, it is also easy to obtain the displacement field and the elastic energy, which are often of interest. In addition, the method can be readily generalized to solve elasticity problems with displacement (or mixed displacement-traction) boundary conditions on the void surface, as well as other types of elasticity problems involving spherical-shaped boundaries such as dislocation-inclusion interaction and contact between spheres. The tools developed in this work may also find uses for solving other boundary-value problems beyond elasticity.

3. General solution to the image stress problem with spherical boundary

For an isotropic linear elastic material without body force, the equilibrium condition can be written in terms of the displacement field \mathbf{u} as:

$$\mu \nabla^2 \mathbf{u} + (\lambda + \mu) \nabla (\nabla \cdot \mathbf{u}) = 0 \quad (2)$$

where λ and μ are Lamé constants. We shall consider boundary condition as specified by the traction vector \mathbf{T}^{img} defined on the surface $\partial\Omega$, as shown in figure 1(b).

In general, we solve the image stress problem in the following steps:

1. Based on the Papkovitch-Neuber representation, we find a complete set of fundamental displacement solutions $\mathbf{u}^{(K)}$ that spans the solution space of equation (2). Using the ShElastic toolbox developed in

this work (see Appendix A), the displacement field $\mathbf{u}^{(K)}$, and the corresponding stress field $\boldsymbol{\sigma}^{(K)}$ and traction $\mathbf{T}^{(K)}$ can be automatically generated and expressed as the superposition of spherical harmonic functions Y_l^m (for definitions see Appendix B).

2. The user specified traction boundary condition $\mathbf{T}^{\text{img}}(\theta, \varphi)$ is expanded in terms of the fundamental traction solutions $\mathbf{T}^{(K)}$:

$$\mathbf{T}^{\text{img}}(\theta, \varphi) = \sum_K a_K \mathbf{T}^{(K)}(\theta, \varphi) \quad (3)$$

where a_K are the expansion coefficients. This is accomplished by first expanding \mathbf{T}^{img} as a linear combination of Y_l^m using SHTOOLS (Wieczorek et al., 2016), and then solve a set of linear equations.

3. The image stress solution $\boldsymbol{\sigma}^{\text{img}}$ can be obtained as a linear combination of the stress fields $\boldsymbol{\sigma}^{(K)}$:

$$\boldsymbol{\sigma}^{\text{img}}(r, \theta, \varphi) = \sum_K a_K \boldsymbol{\sigma}^{(K)}(r, \theta, \varphi) \quad (4)$$

4. Similarly, the displacement field \mathbf{u}^{img} in figure 1(b) can be obtained as:

$$\mathbf{u}^{\text{img}}(r, \theta, \varphi) = \sum_K a_K \mathbf{u}^{(K)}(r, \theta, \varphi) \quad (5)$$

5. Finally, after the displacement and the traction on the spherical interface is obtained, the elastic energy $E_{\text{el}}^{\text{img}} \equiv E_{\text{el}}^{\text{tot}} - E_{\text{el}}^{\infty}$ corresponding to the interaction between the dislocation and void can be calculated as:

$$E_{\text{el}}^{\text{img}} = \frac{1}{2} \int_{\partial\Omega} \mathbf{T}^{\infty} \cdot (\mathbf{u}^{\infty} + \mathbf{u}^{\text{img}}) dS \quad (6)$$

where the integral is over the spherical surface. The proof of equation (6) is provided in Appendix C. The integral can be easily evaluated in the spherical harmonics space as 4π times the complex inner product of the spherical harmonics coefficients of \mathbf{T}^{∞} and $\mathbf{u}^{\infty} + \mathbf{u}^{\text{img}}$.

3.1. Represent fundamental solutions in spherical harmonic space

In this section, we describe how to construct the fundamental displacement bases $\mathbf{u}^{(K)}$, the corresponding $\boldsymbol{\sigma}^{(K)}$, and $\mathbf{T}^{(K)}$ fields that span the solution space. In this work, we derive the solution based on the Papkovitch-Neuber representation (Barber 3rd ed., 2009), because the displacement potentials satisfy the Laplace's equation which have the general solution in

terms of spherical harmonic functions. According to the Papkovitch-Neuber solution, the following displacement field satisfies the equilibrium condition (2):

$$\mathbf{u}^{(K)}(r, \theta, \varphi) = \frac{1}{2\mu} [-4(1 - \nu)\boldsymbol{\psi}^{(K)} + \nabla(\mathbf{r} \cdot \boldsymbol{\psi}^{(K)})] \quad (7)$$

where the displacement potential $\boldsymbol{\psi}^{(K)}(r, \theta, \varphi)$ is a harmonic vector field, i.e. every component of $\boldsymbol{\psi}^{(K)}$ satisfies Laplace's equation $\nabla^2 \psi_j^{(K)} = 0$, $j = x, y, z$.

The general solution of Laplace's equation $\nabla^2 \omega(r, \theta, \varphi) = 0$ in spherical coordinates can be represented as a linear combination of spherical harmonic functions times the radial function ($C_{lm}^R r^l + C_{lm}^I r^{-l-1}$):

$$\omega(r, \theta, \varphi) = \sum_{l=0}^{\infty} \sum_{m=-l}^{+l} \left(C_{lm}^R r^l + \frac{C_{lm}^I}{r^{l+1}} \right) Y_l^m(\theta, \varphi) \quad (8)$$

where C_{lm}^R and C_{lm}^I are constant coefficients, and $Y_l^m(\theta, \varphi)$ are the spherical harmonic functions with two angular indices (l, m). Since there are multiple conventions in the literature, the precise definition of Y_l^m used in this work is provided in Appendix B.1. For the image stress of a spherical void in an infinite continuum, the r^l terms can be eliminated since the solution should decay to zero as $r \rightarrow \infty$. Therefore, we choose the bases of the displacement potential as:

$$\boldsymbol{\psi}^{(K)} = \boldsymbol{\psi}^{(k,l,m)}(r, \theta, \varphi) = \hat{\mathbf{e}}_k \frac{1}{r^{l+1}} Y_l^m(\theta, \varphi) \quad (9)$$

where $\hat{\mathbf{e}}_k$ is the unit vector in the k -th direction ($k = x, y, z$). Here we use index (K) as a short-hand notation for 3-integer indices (k, l, m). The completeness of this solution to the elasticity equation is proved in Appendix A.1. In this work, we only discuss the spherical void problem. However, adding the r^l terms in the fundamental solution bases would lead to a solution applicable to linear elasticity problems in solid spheres and spherical inclusions.

Given a displacement potential basis $\boldsymbol{\psi}^{(K)}$, we can derive the displacement $\mathbf{u}^{(K)}(r, \theta, \varphi)$, the corresponding stress field $\boldsymbol{\sigma}^{(K)}(r, \theta, \varphi)$, and the traction vector $\mathbf{T}^{(K)}(\theta, \varphi)$ on the spherical surface $r = r_0$ in the following form:

$$u_j^{(K)} = u_j^{(k,l,m)} = \frac{1}{2\mu r^{l+1}} U_j^{(K)}(\theta, \varphi) \quad (10)$$

$$\sigma_{ij}^{(K)} = \sigma_{ij}^{(k,l,m)} = \frac{1}{r^{l+2}} S_{ij}^{(K)}(\theta, \varphi) \quad (11)$$

$$T_j^{(K)} = T_j^{(k,l,m)} = \frac{1}{r_0^{l+2}} F_j^{(K)}(\theta, \varphi) \quad (12)$$

where $U_j^{(K)}, S_{ij}^{(K)}, F_j^{(K)}$, ($i, j = x, y, z$) are the r -independent parts of displacement, stress, and traction respectively. Since any complex square-integrable function of (θ, ϕ) can be expressed as a linear combination of Y_l^m (equation (B.15)), the orientation-dependence of the displacement $U_j^{(K)}(\theta, \varphi)$ can be represented as:

$$U_j^{(K)}(\theta, \varphi) = \sum_{l'=0}^{l'_{\max}} \sum_{m'=-l'}^{l'} \hat{U}_{jl'm'}^K Y_{l'}^{m'}(\theta, \varphi) \quad (13)$$

where $\hat{U}_{jl'm'}^K$ are the spherical harmonic expansion coefficients. Similarly, we can express the stress and traction in terms of spherical harmonics with expansion coefficients $\hat{S}_{ijl'm'}^K, \hat{F}_{jl'm'}^K$. In addition, we use indices (J) and (I) as the shorthand notations for (j, l', m') and (i, j, l', m') respectively, so that the displacement, stress and traction fields can be represented by the expansion coefficients $\hat{U}_J^K, \hat{S}_I^K, \hat{F}_I^K$. These constant coefficients can be precomputed given the elastic constants μ and ν , and can be used repeatedly for solving the image stress problem over multiple DD time-steps. The coefficients can be represented as a sparse matrix with K as column index and J (or I) as row index.

The elementary operations needed for calculating the spherical harmonic expansion coefficients are the product of two functions and the spatial gradient of a function. For this purpose, we develop the ShElastic toolbox to obtain these coefficients analytically. Based on these two linear operations, the toolbox is able to calculate the spherical harmonic representation of displacement, stress, and traction based on the spherical harmonic bases of the displacement potential $\psi^{(K)}$. In addition, the toolbox can be easily applied to other differential equations such as Love's solution for linear elasticity problems, or partial differential equations beyond elasticity (such as heat and electromagnetism). The detailed derivation of the toolbox is discussed in Appendix A.

3.2. Solve the image stress problem in spherical harmonic space

To simplify the notation, we express the radial coordinate r in units of the void radius r_0 , i.e. $r^* = r/r_0$. Then the boundary condition set by the image traction vector $\mathbf{T}^{\text{img}}(\theta, \varphi)$ can be sampled on a $n \times 2n$ regular mesh of the unit-sphere surface with $r^* = 1$. The image stress and the displacement at any arbitrary point (x, y, z) can be evaluated with scaled coordinates on the unit sphere, i.e. $\sigma_{ij}^{\text{img}}(x, y, z) = \tilde{\sigma}_{ij}^{\text{img}}(x^*, y^*, z^*)$, $u_j^{\text{img}}(x, y, z) = \tilde{u}_j^{\text{img}}(x^*, y^*, z^*)$, where $x^* = x/r_0$, $y^* = y/r_0$, $z^* = z/r_0$.

We assume every component of traction $T_j^{\text{img}}(\theta, \varphi)$, ($j = x, y, z$) is a square-integrable function, so that we can obtain the spherical harmonics coefficients through numerical spherical harmonic transform algorithms such as SHTOOLS with the maximum degree $l'_{\text{max}} = n/2$:

$$T_j^{\text{img}}(\theta, \varphi) = \sum_{l'=0}^{l'_{\text{max}}} \sum_{m'=-l'}^{l'} \hat{T}_{jl'm'}^{\text{img}} Y_{l'}^{m'}(\theta, \varphi) \quad (14)$$

Again, we will use (J) to represent the indices (j, l', m') . With the spherical harmonics coefficients \hat{T}_J^{img} and the coefficients matrix \hat{F}_J^K of the fundamental solutions given in equation (12), we can express the traction boundary condition (3) in the following form:

$$\sum_{l'} \sum_{m'} \hat{T}_J^{\text{img}} Y_{l'}^{m'} = \sum_K a_K \sum_{l'} \sum_{m'} \hat{F}_J^K Y_{l'}^{m'} \quad (15)$$

which leads to,

$$\hat{T}_J^{\text{img}} = \sum_K \hat{F}_J^K a_K \quad (16)$$

where the coefficients a_K can be solved from the set of linear equations (16). Finally, the image stress solution can be reconstructed using the coefficients a_K :

$$\tilde{\sigma}_{ij}^{\text{img}}(r^*, \theta, \varphi) = \sum_{l'=0}^{l'_{\text{max}}} \sum_{m'=-l'}^{l'} \hat{\sigma}_{ijl'm'}^{\text{img}}(r^*) Y_{l'}^{m'}(\theta, \varphi) \quad (17)$$

where the coefficients are given by

$$\hat{\sigma}_{ijl'm'}^{\text{img}}(r^*) = \hat{\sigma}_I^{\text{img}}(r^*) = \sum_K \frac{a_K}{(r^*)^{l+2}} \hat{S}_I^K \quad (18)$$

Therefore, the image stress field $\boldsymbol{\sigma}^{\text{img}}$ at an arbitrary point (r, θ, φ) can be obtained by inverse spherical harmonic transform (equation (17)) using SHTOOLS, i.e. by superposition of the spherical harmonics with coefficients $\hat{\sigma}_{ijl'm'}^{\text{img}}(r^*)$ evaluated at $r^* = r/r_0$.

Similarly, the image displacement field can be obtained by superposing the fundamental solutions $\mathbf{u}^{(K)}$ as:

$$\tilde{u}_j^{\text{img}}(r^*, \theta, \varphi) = \sum_{l'=0}^{l'_{\text{max}}} \sum_{m'=-l'}^{l'} \hat{u}_{jl'm'}^{\text{img}}(r^*) Y_{l'}^{m'}(\theta, \varphi) \quad (19)$$

where the coefficients are given by

$$\hat{u}_{jl'm'}^{\text{img}}(r^*) = \hat{u}_J^{\text{img}}(r^*) = \sum_K \frac{a_K}{(r^*)^{l+1}} \hat{U}_J^K \quad (20)$$

4. Numerical results

To verify the convergence and accuracy of the image stress method introduced above, we present three test cases for computing the image stress produced by (1) external loading, (2) an infinite straight screw dislocation, and (3) a prismatic dislocation loop, respectively. In the test case (3), we obtain the accurate numerical solution of the glide and climb forces on the prismatic dislocation loop size smaller and larger than the void size, which verifies the qualitative analysis by Willis and Bullough (1969).

In addition, to illustrate the efficiency and accuracy of our method, we perform FEM calculations with ABAQUS (2017) running in serial mode. The FEM geometry takes the shape of a large cube containing a small spherical void and is discretized with second-order tetrahedral elements. The cube is 50 times larger than the void to minimize the external boundary effects of the cubic surfaces. The elements are refined around the spherical void and then gradually coarsened away from the void. The image stress values are obtained on Gauss points and then linearly interpolated along points of interest to compare with the spherical harmonics solution.

Both the spherical harmonic image stress solver (using pre-computed coefficients from ShElastic) and the FEM calculations are performed on a personal computer running Ubuntu16.04. The spherical harmonics method is implemented in python3.6 and the sparse matrix solver is provided by numpy1.13 and scipy1.0.

4.1. Test case 1 – Spherical void subjected to tensile load

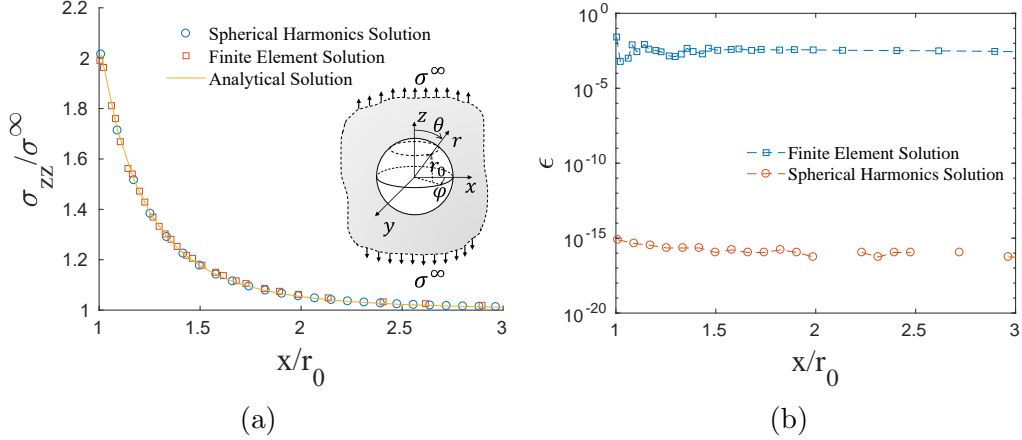


Figure 2: Spherical void in an infinite medium under tension. (a) Stress field $\sigma_{zz}(r)$ on the x - y plane ($z = 0$) from spherical harmonics method, finite element method, and analytic solution. The inset shows a sketch of the geometry. (b) Relative error of the numerical solutions against the analytic solution

We first consider the problem of a spherical void in an isotropic medium under uniaxial tension, as shown in figure 2. The analytical solution of the stress field $\sigma_{zz}(r)$ on the x - y plane ($z = 0$) is given by Sadd (2014):

$$\sigma_{zz} = \sigma^\infty \left[1 + \frac{(4 - 5\nu)}{2(7 - 5\nu)} \left(\frac{r_0}{r}\right)^3 + \frac{9}{2(7 - 5\nu)} \left(\frac{r_0}{r}\right)^5 \right] \quad (21)$$

where σ^∞ is the applied tensile stress; r_0 is the radius of the void; ν is the Poisson's ratio of the elastic medium.

To utilize our spherical harmonic solution, we first perform spherical harmonic decomposition of the image traction boundary condition on the void surface according to the equation (B.6):

$$\mathbf{T}^{\text{img}} = -\mathbf{T}^\infty = -\hat{\mathbf{e}}_z \sigma^\infty \cos \theta = -\hat{\mathbf{e}}_z \sigma^\infty \sqrt{1/3} Y_1^0(\theta, \phi) \quad (22)$$

The parameters in the calculation are taken as $\nu = 1/3$, $\sigma^\infty = 1$, $r_0 = 1$. The solution of the linear set of equations (16), i.e. the coefficients a_K , is given in Table (1).

The solution converges with 10 modes ($l_{\text{max}} = 3$), and the modes with higher l have zero coefficients. The total stress field can be evaluated as follows:

k index	Y_l^m index	Coefficient $a_K = a_{klm}$
x	Y_1^{-1}	-0.04523
	Y_1^1	0.04523
	Y_3^{-1}	-0.02166
	Y_3^1	0.02166
y	Y_1^{-1}	-0.04523 i
	Y_1^1	-0.04523 i
	Y_3^{-1}	-0.02166 i
	Y_3^1	-0.02166 i
z	Y_1^0	-0.2067
	Y_3^0	0.03752

Table 1: Non-zero coefficients in the spherical harmonic solution of image stress produced by tensile loading

$$\boldsymbol{\sigma} = (\hat{\mathbf{e}}_z \otimes \hat{\mathbf{e}}_z)\boldsymbol{\sigma}^\infty + \boldsymbol{\sigma}^{\text{img}} = (\hat{\mathbf{e}}_z \otimes \hat{\mathbf{e}}_z)\boldsymbol{\sigma}^\infty + \sum_K a_K \boldsymbol{\sigma}^{(K)}$$

We compare the stress on the x - y plane with the analytical solution and FEM in figure 2. FEM calculations of the image stress problem was performed with 84175 tetrahedral elements and a total of 354300 degrees of freedom. FEM has an maximum relative error of 3% with a computation time of 460 s. In comparison, the spherical harmonics image stress solver is able to reach the error of 3.5×10^{-15} with the simulation time of 0.026 s. Therefore, our method is able to reach high accuracy with smaller sparse system, and thus higher efficiency compared with FEM.

4.2. Test case 2 – Interaction between a void and a straight dislocation

Gavazza and Barnett (1974) and Willis et al. (1972) developed analytical solutions independently, to the problem of the interaction between a spherical inclusion (with elastic constants λ_2, μ_2) and an infinite long straight screw dislocation in an isotropic infinite medium (with elastic constants λ_1, μ_1). These solutions reduce to the case of dislocation-void interaction in the limit of $\lambda_2, \mu_2 \rightarrow 0$. The geometry of the problem is shown in the inset of figure 3a.

According to the symmetry of the problem, the Peach-Koehler force \mathbf{f} given in equation (1) is only in the x -direction, and is a function of the void-dislocation distance t and coordinate z along the dislocation line: $f_x(t, z) = b \sigma_{yz}^{\text{img}}(t, 0, z)$, where b is the magnitude of the Burger’s vector and

σ^{img} is the image stress induced by the dislocations interacting with the void surface. The analytical solution of the image stress $\sigma_{yz}^{\text{img}}(x, y, z)$ is given in Gavazza and Barnett (1974).

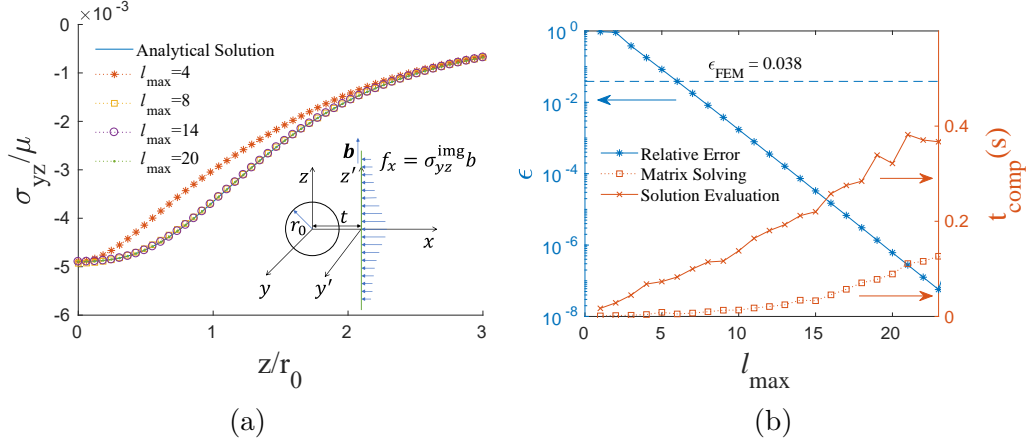


Figure 3: Comparison of spherical harmonics solution and analytical solution. (a) Image stress component σ_{yz}^{img} along the dislocation. Inset shows a sketch of the geometry. (b) Relative error ϵ and computation time t_{comp} for different truncation values l_{max} . The relative error of finite-element method ϵ_{FEM} is marked as dashed line for comparison.

In this test case, we set $\mu = 52.5$ GPa, $\nu = 1/3$, $t/r_0 = 1.5$, $r_0 = 1.25$ nm, and $b = 0.25$ nm (Steinmetz et al., 2013). The stress field of the dislocation in an infinite medium is:

$$\sigma_{xz}^{\infty} = -\frac{\mu b}{2\pi} \frac{y}{(x-t)^2 + y^2}, \quad \sigma_{yz}^{\infty} = \frac{\mu b}{2\pi} \frac{x-t}{(x-t)^2 + y^2}$$

We truncate the solution to a finite series of spherical harmonics to achieve the required accuracy and efficiency. We truncate degree l up to a maximum value l_{max} , and for each l we include all the m values, $-l \leq m \leq l$, to preserve the spherical symmetry. Figure 3a shows the image shear stress σ_{yz}^{img} with different l_{max} . At $l_{\text{max}} = 20$, the image stress computed by the numerical method agrees with the analytic solution very well. Figure 3b shows that the relative error compared to the analytical solution decreases exponentially with increasing l_{max} .

Figure 3b also shows that the matrix solving time increases quadratically with l_{max} , and the solution evaluation time only increases linearly with l_{max} . The quadratic scaling of the matrix solving time is consistent with the dimension (or rank) of the sparse matrix \hat{F}_J^K , which is on the order of $(l_{\text{max}} + 1)^2$.

According to equation (4), the coefficients $\hat{\sigma}_{ijl'm'}^{\text{img}}(r^*)$ depends on the r^{l+1} , where l is the second index of the fundamental solution $(K) = (k, l, m)$. The linear scaling of the solution evaluation time with l_{max} is due to the implementation in which the solutions with the same l -index are grouped and evaluated together. Figure 3b shows that the method converges rapidly as l_{max} increases. For the case of $t/r_0 = 1.5$ with $l_{\text{max}} = 20$, our method already reaches a relative error of 10^{-6} using only 0.38 s of computation time.

For comparison, we also performed FEM simulation of the void-dislocation interaction at $t/r_0 = 1.5$. In order to reach an acceptable accuracy, 84175 tetrahedral elements are used. The maximum relative error of the image stress calculated by FEM is marked as a blue dashed line in figure 3b for comparison with the spherical harmonics method. The relative error of the FEM solution can be as high as 3.8%, and the calculation takes 387 s. Our spherical harmonics method outperforms the FEM method on both accuracy and efficiency by almost four orders of magnitude in the void-dislocation interaction calculation. We expect our method to achieve even higher efficiency with a C or Fortran implementation, which would significantly improve the efficiency of DD simulation of void growth problems.

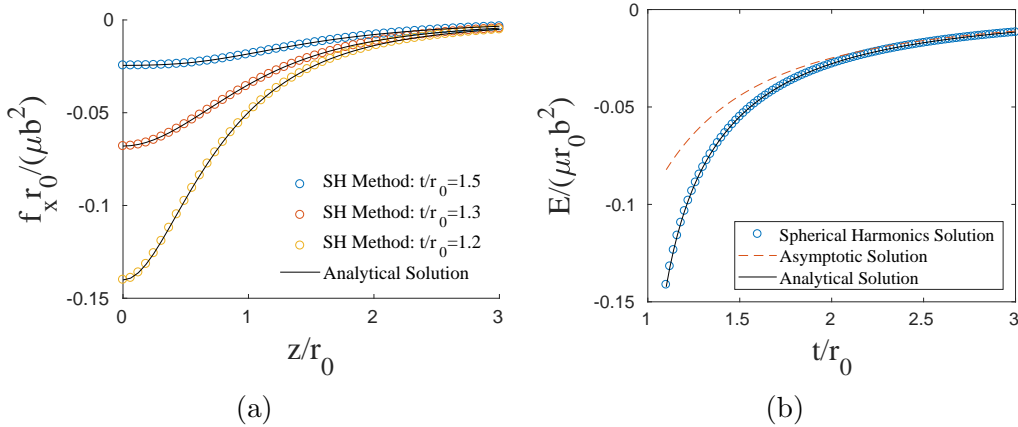


Figure 4: Void-dislocation interaction along the dislocation with different stand-off distance t . (a) Interaction force $f_x(t, z) = b \sigma_{yz}^{\text{img}}(t, 0, z)$ along the dislocation. Stars: numerical solution from this work. Lines: analytic expression from Gavazza and Barnett (1974). (b) Image elastic energy $E_{\text{el}}^{\text{img}}$ as a function of the stand-off distance t . Circles: numerical solution from this work. Solid line: analytic expression from Willis et al. (1972). Dashed line: asymptotic interaction energy given by equation (23).

Figure 4(a) plots the Peach-Koehler force from the image stress on the dis-

location line. Very good agreement is observed between our numerical results and the analytic solution Gavazza and Barnett (1974). To further validate our method, we calculate the image energy $E_{\text{el}}^{\text{img}}$, which is the interaction energy between the dislocation and the void, as a function of the stand-off distances t . The analytic expression of $E_{\text{el}}^{\text{img}}$ can be obtained from the more general result in Willis et al. (1972). The leading term can be written in the explicit form:

$$E^{\text{asy}}(t) = -\frac{5\mu b^2 r_0^3}{2\pi t^2} \frac{1-\nu}{7-5\nu} \quad (23)$$

This is the dominant term at large t , and will be referred to as the asymptotic image energy. The $1/t^2$ scaling of the asymptotic image energy is expected because the stress field of the dislocation scales as $1/t$ so that the elastic energy stored in a spherical volume of an infinite medium should scale as $1/t^2$ for very large t .

Figure 4(b) compares our numerical results for the image energy $E_{\text{el}}^{\text{img}}$ against the analytic expression. Again, very good agreement is observed between the two; the maximum relative error is less than 0.8% at $t = 1.1 r_0$ with $l_{\text{max}} = 20$. While the asymptotic expression provides a good description for the dislocation-void interaction energy at large t , it significantly underestimates the magnitude of the interaction at small stand-off distances (e.g. by $\sim 12\%$ for $t < 1.5 r_0$).

4.3. Test case 3 – Interaction between void and a prismatic dislocation loop

One of the key mechanisms of void growth is the interaction between the void and a nearby prismatic dislocation loop (PDL) (Lubarda et al., 2004). Several analytical methods have been proposed to model this interaction and its relation to void growth, such as Ahn et al. (2006). In this section, we couple our image stress solver to a DD simulation program, DDLab (Cai et al., 2006), to demonstrate the capabilities of our approach.

The coupling between our solver and the DD simulation is achieved as follows. In every iteration, we let DDLab export the stress field of the dislocation in an infinite medium and calculate the traction force on the void surface. We then feed the negative traction force as the boundary condition to spherical harmonics solver to obtain the image stress solution σ^{img} . Finally, we evaluate the Peach-Koehler forces acting on the dislocation segments and add their contributions to the nodal forces calculated by DDLab, and let the DD simulation evolve.

We performed two DD simulations of a PDL in the neighborhood of the void, with the loop radius $\rho_0 = 0.75 r_0$ (the loop is smaller than the void) and $\rho_0 = 1.2 r_0$ (the loop is larger than the void). The elastic properties for the medium are $\mu = 52.5$ GPa, $\nu = 1/3$, same as in Section 4.2. We only consider the glide motion of the loop so that the loop radius remains constant in the simulation. In addition, we do not consider the applied stress σ^{app} and only consider the effect of the image stress σ^{img} on the dislocation loop.

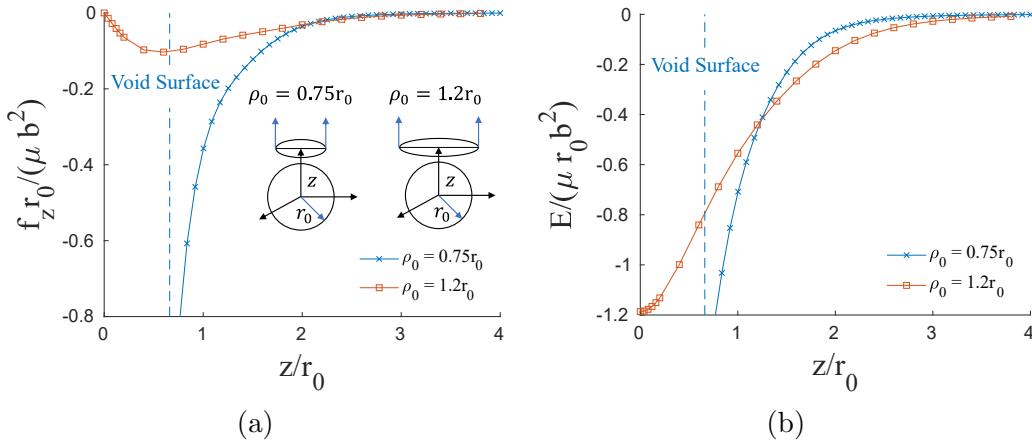


Figure 5: The simulation result for PDLs whose radius ρ_0 are 0.75 and 1.2 times the void radius r_0 . (a) Normalized glide forces $f_z r_0 / (\mu b^2)$. The inset shows sketches of the geometry, and the arrows indicates the positive direction of the force f_z . (b) Normalized interaction energy $E_{\text{el}}^{\text{img}} / (\mu r_0 b^2)$ between the void and the dislocation loop. The dashed line indicates the void surface when $\rho_0 = 0.75 r_0$.

Figure 5a shows the glide forces of the PDL with different radius values ($0.75 r_0$ and $1.2 r_0$). The dislocations are always attracted towards the center of the void. For the case of the PDL with radius less than the void, the dislocation loop accelerates when getting closer to the void surface. The force reaches negative infinity when the loop is approaching the void surface. For the case of the PDL with the radius larger than the void, the dislocation loop initially accelerates as it moves from far away towards the void surface. Then, the loop decelerates and finally stops at $z = 0$, forming a “Saturn ring” around the void. The results are consistent with the qualitative analyses by Willis and Bullough (1969).

In addition, the image elastic energy is evaluated during the simulation, as shown in figure 5a. The interaction energy for the loop with radius $\rho_0 = 0.75 r_0$ keeps decreasing towards negative infinity as the dislocation

loop approaches the void surface, while the interaction energy for the loop with radius $\rho_0 = 1.2 r_0$ radius reaches a minimum at $z = 0$. These results are consistent with the behaviors of the PDL in the simulation. We have also verified (by numerical differentiation) that the glide force and the image elastic energy satisfy the following relation:

$$f_z(z) \cdot 2\pi\rho_0 \equiv F_z^{\text{img}}(z) = -\frac{\partial E_{\text{el}}^{\text{img}}(z)}{\partial z} \quad (24)$$

where F_z^{img} is the total glide force on the dislocation loop due to the image stress.

5. Discussions and conclusions

In the present work, we develop an image stress solver for arbitrary tractions on spherical voids. Based on the expansion of the displacement potentials in the Papkovitch-Neuber representation of the isotropic elasticity problem, the image stress solver outperforms the finite-element method (FEM) in terms of both efficiency and accuracy. Our method is also expected to be more efficient than the boundary element method (BEM). The stiffness matrix in BEM is usually a dense matrix, which implies that the time to solve the linear system grows with the square of the matrix size (number of boundary element nodes). However, F_J^K is a sparse matrix in our method, thus the time to solve the linear system grows only linearly with the matrix size (number of fundamental bases).

We have demonstrated that the spherical harmonics image stress solver can be coupled with the DD model to simulate void-dislocation interaction. The method can also be readily generalized for solving other elasticity problems with spherical boundaries. For example to model the growth of Helium bubbles inside irradiated metals (Misra et al., 2007), the boundary condition can be changed to constant pressure (instead of zero traction) on the spherical surface. In addition, by changing the radius-dependent factor $1/r^{l+1}$ to r^l when constructing the fundamental basis $\psi^{(K)}$, the method can be used for solving the contact problem between spheres. Keeping both $1/r^{l+1}$ and r^l terms would enable efficient solutions for dislocation interaction with inclusions and inhomogeneities.

Acknowledgements

The authors are grateful for the help from Dr. Chao Pu (AK Steel Corp) in setting up the dislocation-void interaction FEM simulation in ABAQUS, and useful discussions about the spherical harmonics analysis with Dr. Yang Zhou (Department of Mathematics, Stanford University). This work was supported by the U.S. Department of Energy, Office of Basic Energy Sciences, Division of Materials Sciences and Engineering under Award No. de-sc0010412.

Appendix A. Spherical harmonic coefficients for fundamental elasticity solutions

In section 3, we express the displacement potential $\boldsymbol{\psi}^{(K)}$, the corresponding $\mathbf{u}^{(K)}$, $\boldsymbol{\sigma}^{(K)}$ and $\mathbf{T}^{(K)}$ fields in terms of the product of a pre-factor $f(r)$ and a radius-independent part $U_j^K(\theta, \varphi)$, $S_{ij}^K(\theta, \varphi)$, $F_j^K(\theta, \varphi)$ in equations (10,11,12). These radius independent functions can then be represented as linear combinations of spherical harmonic functions, for example equation (13). In this section, we will show how we obtain the expansion coefficients $\hat{U}_{jl'm'}^K$, $\hat{S}_{ijl'm'}^K$, $\hat{F}_{jl'm'}^K$ starting from the spherical harmonics representation of displacement potential $\boldsymbol{\psi}^{(K)}$. These functions are implemented in ShElastic toolbox and the coefficients up to $l_{\max} = 40$ are pre-calculated and saved as a sparse matrix.

Appendix A.1. Completeness of spherical harmonics solution

The Papkovitch-Neuber solution is a general solution to the equilibrium condition (2) without rigid-body motion and rotation (Barber 3rd ed., 2009), and can be written in terms of displacement potential vector $\boldsymbol{\psi}$ and function ϕ :

$$2\mu\mathbf{u} = -4(1 - \nu)\boldsymbol{\psi} + \nabla(\mathbf{r} \cdot \boldsymbol{\psi} + \phi) \quad (\text{A.1})$$

where both $\boldsymbol{\psi}$ and ϕ are harmonic, i.e., satisfying Laplace's equation $\nabla^2\psi_j = 0$, ($j = x, y, z$); $\nabla^2\phi = 0$. Similar to section 3.1, we can choose the basis functions for the displacement potentials $\boldsymbol{\psi}^{(k,l,m)}$ and $\phi^{(l',m')}$ as the general solution to the Laplace's equation:

$$\boldsymbol{\psi}^{(k,l,m)} \equiv \frac{1}{r^{l+1}} \hat{\mathbf{e}}_k Y_l^m(\theta, \varphi), \quad \phi^{(l',m')} \equiv \frac{1}{r^{l'+1}} Y_{l'}^{m'}(\theta, \varphi) \quad (\text{A.2})$$

so that they completely span the solution space of the spherical void problem. However, in equation (7), we only choose the $\boldsymbol{\psi}$ terms as the fundamental bases. In the following, We will show that such an expansion is still complete, by proving that $\phi^{(l',m')}$ can be written as a linear combination of $\boldsymbol{r} \cdot \boldsymbol{\psi}^{(k,l,m)}$.

Given the definition of $\boldsymbol{\psi}^{(k,l,m)}$ and $\phi^{(l',m')}$, we have

$$\boldsymbol{r} \cdot \boldsymbol{\psi}^{(k,l,m)} = x_k \frac{Y_l^m}{r^{l+1}}, \quad \phi^{(l-1,m)} = \frac{Y_{l-1}^m}{r^l} \quad (l \geq 1) \quad (\text{A.3})$$

We will show that $\phi^{(l-1,m)}$ can be written as a linear combination of $\boldsymbol{r} \cdot \boldsymbol{\psi}^{(k,l,m)}$. Because $Y_1^1 = \sqrt{3/2}(x+iy)/r$ and $Y_1^0 = \sqrt{3}z/r$ (see equations(B.5)-(B.7)), we have (for $-l+1 \leq m \leq l$)

$$\begin{bmatrix} \boldsymbol{r} \cdot \boldsymbol{\psi}^{(x,l,m-1)} + i\boldsymbol{r} \cdot \boldsymbol{\psi}^{(y,l,m-1)} \\ \sqrt{2}\boldsymbol{r} \cdot \boldsymbol{\psi}^{(z,l,m)} \end{bmatrix} = \frac{1}{r^l} \sqrt{\frac{2}{3}} \begin{bmatrix} Y_l^{m-1} Y_1^1 \\ Y_l^m Y_1^0 \end{bmatrix} \quad (\text{A.4})$$

In Appendix B we show how the products of spherical harmonic functions can be written as linear combinations of Y_l^m . Specifically, equation (B.23) leads to the following linear equations:

$$\begin{bmatrix} Y_l^{m-1} Y_1^1 \\ Y_l^m Y_1^0 \end{bmatrix} = \boldsymbol{C}^- \begin{bmatrix} Y_{l+1}^m \\ Y_{l-1}^m \end{bmatrix} \equiv \begin{bmatrix} C_{(l,1)}^{(m-1,1)} & C_{(l,-1)}^{(m-1,1)} \\ C_{(l,1)}^{(m,0)} & C_{(l,-1)}^{(m,0)} \end{bmatrix} \begin{bmatrix} Y_{l+1}^m \\ Y_{l-1}^m \end{bmatrix} \quad (\text{A.5})$$

Because of the orthogonality of Clebsch-Gordan coefficients (Varshalovich et al., 1989), \boldsymbol{C}^- is a nonsingular matrix, i.e. it can be inverted. Therefore (for $-l+1 \leq m \leq l$), we can obtain Y_{l-1}^m by solving the equation (A.5):

$$\phi^{(l-1,m)} = \frac{Y_{l-1}^m}{r^l} = \frac{1}{|\boldsymbol{C}^-| r^l} \left[C_{(l,-1)}^{(m,0)} (Y_l^m Y_1^0) - C_{(l,1)}^{(m,0)} (Y_l^{m-1} Y_1^1) \right] \quad (\text{A.6})$$

where $|\boldsymbol{C}^-|$ is the determinant of matrix \boldsymbol{C}^- . Given equation (A.4), $\phi^{(l-1,m)}$ is now expressed as a linear combination of $\boldsymbol{r} \cdot \boldsymbol{\psi}^{(x,l,m-1)}$, $\boldsymbol{r} \cdot \boldsymbol{\psi}^{(y,l,m-1)}$, and $\boldsymbol{r} \cdot \boldsymbol{\psi}^{(z,l,m)}$.

Similarly, for $-l \leq m \leq l-1$ we have

$$\begin{bmatrix} \boldsymbol{r} \cdot \boldsymbol{\psi}^{(x,l,m+1)} - i\boldsymbol{r} \cdot \boldsymbol{\psi}^{(y,l,m+1)} \\ \sqrt{2}\boldsymbol{r} \cdot \boldsymbol{\psi}^{(z,l,m)} \end{bmatrix} = \frac{1}{r^l} \sqrt{\frac{2}{3}} \begin{bmatrix} Y_l^{m+1} Y_1^{-1} \\ Y_l^m Y_1^0 \end{bmatrix} \quad (\text{A.7})$$

where

$$\begin{bmatrix} Y_l^{m+1} Y_1^{-1} \\ Y_l^m Y_1^0 \end{bmatrix} = \boldsymbol{C}^+ \begin{bmatrix} Y_{l+1}^m \\ Y_{l-1}^m \end{bmatrix} \equiv \begin{bmatrix} C_{(l,1)}^{(m+1,-1)} & C_{(l,-1)}^{(m+1,-1)} \\ C_{(l,1)}^{(m,0)} & C_{(l,-1)}^{(m,0)} \end{bmatrix} \begin{bmatrix} Y_{l+1}^m \\ Y_{l-1}^m \end{bmatrix} \quad (\text{A.8})$$

which allows us to show that

$$\phi^{(l-1,m)} = \frac{Y_{l-1}^m}{r^l} = \frac{1}{|\mathbf{C}^+| r^l} \left[C_{(l,-1)}^{(m,0)} (Y_l^m Y_1^0) - C_{(l,1)}^{(m,0)} (Y_l^{m+1} Y_1^{-1}) \right] \quad (\text{A.9})$$

so that $\phi^{(l-1,m)}$ is now expressed as a linear combination of $\mathbf{r} \cdot \boldsymbol{\psi}^{(x,l,m+1)}$, $\mathbf{r} \cdot \boldsymbol{\psi}^{(y,l,m+1)}$, and $\mathbf{r} \cdot \boldsymbol{\psi}^{(z,l,m)}$. This proves that the expansion of the vector potential $\boldsymbol{\psi}$ alone into spherical harmonics completely spans the solution space.

Appendix A.2. Displacement solution

In this section, we will show how we obtain the radius independent part of the displacement basis $U_j^K(\theta, \varphi)$ and thus the expansion coefficients $\hat{U}_{jl'm'}^K$. Based on the fundamental bases of the displacement potential function (9), the displacement solution $\mathbf{u}^{(k,l,m)} = \mathbf{u}^{(K)}$ can be written as:

$$2\mu \mathbf{u}^{(K)} = -4(1-\nu) \hat{\mathbf{e}}_k \frac{Y_l^m}{r^{l+1}} + \nabla \left(\frac{x_k Y_l^m}{r^{l+1}} \right) \quad (\text{A.10})$$

The first term is already represented in terms of spherical harmonic functions. To expand the second term, it is convenient to introduce the first and second vector spherical harmonics (VSH), \mathbf{Y}_l^m and $\boldsymbol{\Psi}_l^m$,

$$\mathbf{Y}_l^m \equiv Y_l^m \hat{\mathbf{r}} \quad (\text{A.11})$$

$$\boldsymbol{\Psi}_l^m \equiv r \nabla Y_l^m \quad (\text{A.12})$$

where $\hat{\mathbf{r}} = [x/r, y/r, z/r]^T$ is the unit vector in the radial direction. Both \mathbf{Y}_l^m and $\boldsymbol{\Psi}_l^m$ are independent of r , so they can be expressed as linear combinations of Y_l^m , as shown in equations (B.18) and (B.19).

For brevity, we introduce coefficients $Q_{klm}^{l'm'}$ to describe the relationship between \mathbf{Y}_l^m and Y_l^m ,

$$[\mathbf{Y}_l^m(\theta, \varphi)]_k = \sum_{l',m'} Q_{klm}^{l'm'} Y_{l'}^{m'}(\theta, \varphi) \quad (\text{A.13})$$

where $[\mathbf{Y}_l^m(\theta, \varphi)]_k$ is the k -th component of \mathbf{Y}_l^m . Given these definitions, we

can rewrite the displacement solution as

$$\begin{aligned}
2\mu u_j^{(K)} &= -4(1-\nu) \delta_{jk} \frac{1}{r^{l+1}} Y_l^m + \frac{\partial}{\partial x_j} \left(\frac{1}{r^l} [\mathbf{Y}_l^m]_k \right) \\
&= -4(1-\nu) \delta_{jk} \frac{1}{r^{l+1}} Y_l^m + \sum_{l',m'} Q_{klm}^{l'm'} \frac{\partial}{\partial x_j} \left(\frac{1}{r^{l'}} Y_{l'}^{m'} \right) \\
&= -4(1-\nu) \delta_{jk} \frac{1}{r^{l+1}} Y_l^m + \sum_{l',m'} Q_{klm}^{l'm'} \left(\frac{-l}{r^{l+1}} [\mathbf{Y}_{l'}^{m'}]_j + \frac{1}{r^{l+1}} [\mathbf{\Psi}_{l'}^{m'}]_j \right)
\end{aligned} \tag{A.14}$$

Therefore, the r -independent part of the displacement solution is

$$\begin{aligned}
U_j^K &\equiv 2\mu r^{l+1} u_j^{(K)} = \sum_{l',m'} \hat{U}_{jl'm'}^K Y_{l'}^{m'} \\
&= -4(1-\nu) \delta_{jk} Y_l^m + \sum_{l',m'} Q_{klm}^{l'm'} \left(-l [\mathbf{Y}_{l'}^{m'}]_j + [\mathbf{\Psi}_{l'}^{m'}]_j \right)
\end{aligned} \tag{A.15}$$

Given that the VSH functions \mathbf{Y}_l^m and $\mathbf{\Psi}_l^m$ can be written as linear combination of Y_l^m according to equations (B.18) and (B.19), we now have expressed U_j^K as linear combination of spherical harmonic functions.

Appendix A.3. Stress and traction solution

The spatial gradient of the displacement solution $u_j^{(K)}$ can be expressed as

$$\begin{aligned}
u_{j,i}^{(K)} &= \sum_{l',m'} \hat{U}_{jl'm'}^{klm} \frac{\partial}{\partial x_i} \left(\frac{Y_{l'}^{m'}}{2\mu r^{l+1}} \right) \\
&= \frac{1}{2\mu r^{l+2}} \sum_{l',m'} \hat{U}_{jl'm'}^{klm} \left[-(l+1) [\mathbf{Y}_{l'}^{m'}]_i + [\mathbf{\Psi}_{l'}^{m'}]_i \right]
\end{aligned} \tag{A.16}$$

Similarly, given that the VSH \mathbf{Y}_l^m and $\mathbf{\Psi}_l^m$ can be written as linear combination of Y_l^m according to equations (B.18) and (B.19), we now have expressed the displacement gradient $u_{j,i}^{(K)}$ as linear combination of Y_l^m . The stress field can be calculated through the following constitutive relation:

$$\sigma_{ij}^{(K)} = \lambda u_{u,u}^{(K)} \delta_{ij} + \mu (u_{i,j}^{(K)} + u_{j,i}^{(K)}) \tag{A.17}$$

This allows us to express the r -independent part of the stress field as a linear combination of Y_l^m ,

$$S_{ij}^{(K)} \equiv r^{l+2} \sigma_{ij}^{(K)} = \sum_{l',m'} \hat{S}_{ijl'm'}^{klm} Y_{l'}^{m'} \quad (\text{A.18})$$

Finally, the traction vector of mode (K) at the void surface ($r = r_0$) can be evaluated as:

$$T_j^{(K)} = \sigma_{ij}^{(K)} n_i = -\frac{x_i}{r} \sigma_{ij}^{(K)} = -\frac{1}{r_0^{l+2}} \sum_{l',m'} \sum_i \hat{S}_{ijl'm'}^{klm} [\mathbf{Y}_{l'}^{m'}]_i \quad (\text{A.19})$$

where $\mathbf{n} = -\hat{\mathbf{r}}$ is the normal vector of the void surface. Therefore,

$$\begin{aligned} F_j^{(K)} &\equiv r_0^{l+2} T_j^{(K)} = \sum_{l',m'} \hat{F}_{jl'm'}^{klm} Y_{l'}^{m'} \\ &= -\sum_{l',m'} \sum_i \hat{S}_{ijl'm'}^{klm} [\mathbf{Y}_{l'}^{m'}]_i = -\sum_{l',m'} \sum_{l'',m''} \sum_i \hat{S}_{ijl'm'}^{klm} Q_{il'm''}^{l''m''} Y_{l''}^{m''} \end{aligned} \quad (\text{A.20})$$

Appendix B. Transformation rules for spherical harmonic functions

In Appendix A, we saw that obtaining the coefficients \hat{U}_J^K , \hat{S}_I^K , \hat{F}_J^K requires the expansion of VSH functions \mathbf{Y}_l^m , Ψ_l^m in terms of Y_l^m . In this appendix, we provide explicit expressions for these expansion coefficients and the proof of the expansion. We start with the explicit expressions of the spherical harmonic functions used in this paper, since there are multiple conventions of Y_l^m in the literature.

Appendix B.1. Definitions of spherical harmonic functions

$Y_l^m(\theta, \varphi)$ are the complex spherical harmonic functions defined on the spherical surface, where $\theta \in [0, \pi]$ is the colatitude angle and the $\varphi \in [0, 2\pi]$ is the longitude angle, $l = 0, 1, \dots$, and $m = -l, -l+1, \dots, l$.

$$Y_l^m(\theta, \varphi) = \begin{cases} \sqrt{(2l+1) \frac{(l-m)!}{(l+m)!}} P_{lm}(\cos \theta) e^{im\varphi}, & m \geq 0 \\ (-1)^{|m|} [Y_l^{|m|}(\theta, \varphi)]^*, & m < 0 \end{cases} \quad (\text{B.1})$$

where $[Y_l^{-|m|}]^*$ is the complex conjugate function of $Y_l^{-|m|}$, and $P_{lm}(\mu)$ is the associated Legendre function (without Condon-Shortley phase), which is defined as:

$$P_{lm}(\mu) = (1 - \mu^2)^{m/2} \frac{d^m}{d\mu^m} P_l(\mu) \quad (\text{B.2})$$

$$P_l(\mu) = \frac{1}{2^l l!} \frac{d^l}{d\mu^l} (\mu^2 - 1)^l \quad (\text{B.3})$$

Some examples of the low-order complex spherical harmonics are listed here in both spherical and Cartesian coordinates:

$$Y_0^0 = 1 \quad (\text{B.4})$$

$$Y_1^{-1} = -\sqrt{\frac{3}{2}} e^{-i\varphi} \sin \theta = -\sqrt{\frac{3}{2}} \frac{x - iy}{r} \quad (\text{B.5})$$

$$Y_1^0 = \sqrt{3} \cos \theta = \sqrt{3} \frac{z}{r} \quad (\text{B.6})$$

$$Y_1^1 = \sqrt{\frac{3}{2}} e^{i\varphi} \sin \theta = \sqrt{\frac{3}{2}} \frac{x + iy}{r} \quad (\text{B.7})$$

$$Y_2^{-2} = \frac{\sqrt{30}}{4} e^{-2i\varphi} \sin^2 \theta = \frac{\sqrt{30}}{4} \frac{(x - iy)^2}{r^2} \quad (\text{B.8})$$

$$Y_2^{-1} = -\sqrt{\frac{15}{2}} e^{-i\varphi} \sin \theta \cos \theta = -\sqrt{\frac{15}{2}} \frac{(x - iy)z}{r^2} \quad (\text{B.9})$$

$$Y_2^0 = \frac{\sqrt{5}}{2} (3 \cos^2 \theta - 1) = \frac{\sqrt{5}}{2} \frac{2z^2 - x^2 - y^2}{r^2} \quad (\text{B.10})$$

$$Y_2^1 = \sqrt{\frac{15}{2}} e^{i\varphi} \sin \theta \cos \theta = \sqrt{\frac{15}{2}} \frac{(x + iy)z}{r^2} \quad (\text{B.11})$$

$$Y_2^2 = \frac{\sqrt{30}}{4} e^{2i\varphi} \sin^2 \theta = \frac{\sqrt{30}}{4} \frac{(x + iy)^2}{r^2} \quad (\text{B.12})$$

where the radius $r = \sqrt{x^2 + y^2 + z^2}$.

Two spherical harmonics Y_l^m and $Y_{l'}^{m'}$ satisfy the orthogonality condition with 4π -Geodesy normalization:

$$\int_{\Omega} [Y_l^m(\theta, \varphi)]^* Y_{l'}^{m'}(\theta, \varphi) d\Omega = 4\pi \delta_{ll'} \delta_{mm'} \quad (\text{B.13})$$

The product of two spherical harmonic functions $Y_{l_1}^{m_1}$, $Y_{l_2}^{m_2}$ can be expanded as a linear combination of spherical harmonics:

$$Y_{l_1}^{m_1}(\theta, \varphi)Y_{l_2}^{m_2}(\theta, \varphi) = \sum_{L=|l_1-l_2|}^{|l_1+l_2|} c(l_1, m_1, l_2, m_2, L, M)c(l_1, 0, l_2, 0, L, 0) \sqrt{\frac{(2l_1+1)(2l_2+1)}{2L+1}} Y_L^M(\theta, \varphi) \quad (\text{B.14})$$

where $M = m_1 + m_2$, and $c(l_1, m_1, l_2, m_2, L, M)$ is the Clebsch-Gordan (CG) coefficients (Varshalovich et al., 1989). Note that the CG coefficients for invalid indices such as $M > L$ or $M < -L$ are zero.

Appendix B.2. Expansion into spherical harmonic functions

Any complex square-integrable function on the unit sphere can be expressed in terms of the linear combination of spherical harmonics:

$$\Omega(\theta, \varphi) = \sum_{l=0}^{\infty} \sum_{m=-l}^{+l} \hat{\Omega}_{lm} Y_l^m(\theta, \varphi) \quad (\text{B.15})$$

where $\hat{\Omega}_{lm}$ are the complex spherical harmonic coefficients.

For any complex function in 3D space $\omega(r, \theta, \varphi)$, the spherical harmonic expansion can be written as:

$$\omega(r, \theta, \varphi) = \sum_{l=0}^{\infty} \sum_{m=-l}^{+l} \omega_{lm}(r) Y_l^m(\theta, \varphi) \quad (\text{B.16})$$

where the coefficients $\omega_{lm}(r)$ are functions of r instead of constants.

SHTOOLS (Wieczorek et al., 2016) provides fast forward and backward spherical harmonics transform in the form of equation (B.15). The forward transformation is expanding a discretized 2D-surface function $\Omega(\theta, \varphi)$ to spherical harmonic coefficients $\hat{\Omega}_{lm}$, while the backward transformation is reconstructing the 2d-surface function from the coefficients. For 3D-functions, the spherical harmonic transform can be performed at a specific radius $r = r_0$:

$$\omega(r_0, \theta, \varphi) = \sum_{l=0}^{\infty} \sum_{m=-l}^{+l} \hat{\omega}_{lm}(r_0) Y_l^m(\theta, \varphi) \quad (\text{B.17})$$

Appendix B.3. Vector spherical harmonics

In this work, we make use of vector spherical harmonic functions to simplify the notation. We follow the convention in Barrera et al. (1985): given a scalar spherical harmonic function $Y_l^m(\theta, \varphi)$, the first and second vector spherical harmonics (VSH) are defined by equations (A.11) and (A.12), respectively. Note that both \mathbf{Y}_l^m and Ψ_l^m are functions of θ and φ only, i.e. they are independent of r , similar to Y_l^m .

In this section, we show that the first and second VSH functions, \mathbf{Y}_l^m and Ψ_l^m , can be expressed as linear combinations of Y_l^m as follows:

$$\mathbf{Y}_l^m = \begin{bmatrix} \sqrt{\frac{1}{6}}(C_{(l,1)}^{(m,1)}Y_{l+1}^{m+1} + C_{(l,-1)}^{(m,1)}Y_{l-1}^{m+1}) - C_{(l,1)}^{(m,-1)}Y_{l+1}^{m-1} - C_{(l,-1)}^{(m,-1)}Y_{l-1}^{m-1} \\ \sqrt{\frac{1}{6}}i(C_{(l,1)}^{(m,1)}Y_{l+1}^{m+1} + C_{(l,-1)}^{(m,1)}Y_{l-1}^{m+1} + C_{(l,1)}^{(m,-1)}Y_{l+1}^{m-1} + C_{(l,-1)}^{(m,-1)}Y_{l-1}^{m-1}) \\ \sqrt{\frac{1}{3}}(C_{(l,1)}^{(m,0)}Y_{l+1}^m + C_{(l,-1)}^{(m,0)}Y_{l-1}^m) \end{bmatrix} \quad (\text{B.18})$$

$$\Psi_l^m(\theta, \varphi) = (l+1)\mathbf{Y}_l^m + \frac{1}{2a_l^m} \begin{bmatrix} a_{l+1}^{m-1}Y_{l+1}^{m-1} - a_{l+1}^{m+1}Y_{l+1}^{m+1} \\ i(a_{l+1}^{m-1}Y_{l+1}^{m-1} + a_{l+1}^{m+1}Y_{l+1}^{m+1}) \\ -2a_{l+1}^m Y_{l+1}^m \end{bmatrix} \quad (\text{B.19})$$

where

$$a_l^m \equiv \sqrt{\frac{(l+m)!(l-m)!}{2l+1}} \quad (\text{B.20})$$

Appendix B.3.1. Proof of the first vector spherical harmonics expression

Based on equations (B.5)-(B.7), the unit vector $\hat{\mathbf{r}}$ can be written in terms of Y_l^m as:

$$\hat{\mathbf{r}} = \begin{bmatrix} x/r \\ y/r \\ z/r \end{bmatrix} = \sqrt{\frac{1}{6}} \begin{bmatrix} Y_1^1 - Y_1^{-1} \\ i(Y_1^1 + Y_1^{-1}) \\ \sqrt{2}Y_1^0 \end{bmatrix} \quad (\text{B.21})$$

Therefore, the first VSH function $\mathbf{Y}_l^m(\theta, \phi)$ can be written as:

$$\mathbf{Y}_l^m(\theta, \phi) \equiv Y_l^m \hat{\mathbf{r}} = \sqrt{\frac{1}{6}} \begin{bmatrix} Y_1^1 Y_l^m - Y_1^{-1} Y_l^m \\ i(Y_1^1 Y_l^m + Y_1^{-1} Y_l^m) \\ \sqrt{2}Y_1^0 Y_l^m \end{bmatrix} \quad (\text{B.22})$$

where the product of spherical harmonic functions can be further expressed as linear combination of spherical harmonic functions using equation (B.14). Specifically,

$$\begin{aligned}
Y_l^m Y_1^1 &= C_{(l,1)}^{(m,1)} Y_{l+1}^{m+1} + C_{(l,0)}^{(m,1)} Y_l^{m+1} + C_{(l,-1)}^{(m,1)} Y_{l-1}^{m+1} \\
Y_l^m Y_1^{-1} &= C_{(l,1)}^{(m,-1)} Y_{l+1}^{m-1} + C_{(l,0)}^{(m,-1)} Y_l^{m-1} + C_{(l,-1)}^{(m,-1)} Y_{l-1}^{m-1} \\
Y_l^m Y_1^0 &= C_{(l,1)}^{(m,0)} Y_{l+1}^m + C_{(l,0)}^{(m,0)} Y_l^m + C_{(l,-1)}^{(m,0)} Y_{l-1}^m
\end{aligned} \tag{B.23}$$

where the constants $C_{(l,l')}^{(m,m')}$, ($l', m' = 0, \pm 1$) are:

$$\begin{aligned}
C_{(l,1)}^{(m,\pm 1)} &= \sqrt{\frac{3(l+1)}{2l+3}} c(l, m, 1, \pm 1, l+1, m \pm 1) \\
C_{(l,1)}^{(m,0)} &= \sqrt{\frac{3(l+1)}{2l+3}} c(l, m, 1, 0, l+1, m) \\
C_{(l,-1)}^{(m,\pm 1)} &= \sqrt{\frac{3l}{2l-1}} c(l, m, 1, \pm 1, l-1, m \pm 1) \\
C_{(l,-1)}^{(m,0)} &= \sqrt{\frac{3l}{2l-1}} c(l, m, 1, 0, l-1, m) \\
C_{(l,0)}^{(m,0)} &= C_{(l,0)}^{(m,\pm 1)} = 0
\end{aligned} \tag{B.24}$$

which leads to equation (B.18) that we set out to prove.

Appendix B.3.2. Proof of the second vector spherical harmonics expression

In order to prove equation (B.19), we introduce the irregular solid harmonic function $\mathcal{I}_l^m(r, \theta, \varphi)$, which is defined as:

$$\mathcal{I}_l^m(r, \theta, \varphi) \equiv \begin{cases} \frac{(l-m)!}{r^{l+1}} P_m(\cos \theta) e^{im\varphi}, & m \geq 0 \\ (-1)^{|m|} [\mathcal{I}_l^{|m|}(r, \theta, \varphi)]^*, & m < 0 \end{cases} \tag{B.25}$$

and \mathcal{I}_l^m and Y_l^m are related with:

$$\mathcal{I}_l^m = a_l^m \frac{Y_l^m}{r^{l+1}} \tag{B.26}$$

where a_l^m is defined in equation (B.20).

The second VSH function Ψ_l^m can now be expressed in terms of \mathbf{Y}_l^m and \mathcal{I}_l^m as follows.

$$\begin{aligned}
\Psi_l^m &\equiv r \nabla Y_l^m = \frac{r}{a_l^m} \nabla (r^{l+1} \mathcal{I}_l^m) \\
&= \frac{r}{a_l^m} [(l+1) r^l \hat{\mathbf{r}} \mathcal{I}_l^m + r^{l+1} \nabla \mathcal{I}_l^m] \\
&= (l+1) \mathbf{Y}_l^m + \frac{r^{l+2}}{a_l^m} \nabla \mathcal{I}_l^m
\end{aligned} \tag{B.27}$$

The gradient of \mathcal{I}_l^m can be obtained by Hobson's differentiation (Hobson, 1931):

$$D_1 \mathcal{I}_l^m = \mathcal{I}_{l+1}^{m-1}, \quad D_2 \mathcal{I}_l^m = -\mathcal{I}_{l+1}^{m+1}, \quad D_3 \mathcal{I}_l^m = -\mathcal{I}_{l+1}^m; \tag{B.28}$$

where the differentiation operator D_i is defined as:

$$D_1 \equiv \left(\frac{\partial}{\partial x} - i \frac{\partial}{\partial y} \right), \quad D_2 \equiv \left(\frac{\partial}{\partial x} + i \frac{\partial}{\partial y} \right), \quad D_3 \equiv \frac{\partial}{\partial z}. \tag{B.29}$$

which leads to the gradient of \mathcal{I}_l^m :

$$\nabla \mathcal{I}_l^m = \frac{1}{2} \begin{bmatrix} \mathcal{I}_{l+1}^{m-1} - \mathcal{I}_{l+1}^{m+1} \\ i(\mathcal{I}_{l+1}^{m-1} + \mathcal{I}_{l+1}^{m+1}) \\ -2\mathcal{I}_{l+1}^m \end{bmatrix} \tag{B.30}$$

Plugging equations (B.30) and (B.25) into equation (B.27) leads to the proof of equation (B.19).

Appendix C. Image elastic energy

Here we derive the expression for the image elastic energy in equation (6). For clarity, let us define E_{el}^∞ as the elastic energy of an infinite medium containing dislocations, as shown in figure 1(a). For simplicity, we shall assume that there are no dislocations in the spherical region corresponding to the hole. Let $E_{\text{el}}^{\text{tot}}$ be the elastic energy of interest, for which a spherical hole is carved out of the elastic medium containing the dislocations, as shown in figure 1(c). The image elastic energy is the difference between these two energies, i.e.

$$E_{\text{el}}^{\text{img}} = E_{\text{el}}^{\text{tot}} - E_{\text{el}}^\infty \tag{C.1}$$

The image elastic energy can be considered as the interaction energy between the dislocations and the spherical void. We note that $E_{\text{el}}^{\text{img}}$ has a negative value, corresponding to the attractive nature of the dislocation-void interaction.

We emphasize that $E_{\text{el}}^{\text{img}}$ is *not* the elastic energy $E_{\text{el}}^{(b)}$ of the image stress problem, which is shown in figure 1(b). In other words, while the stress field of Problem (c) in figure 1 can be obtained by superposing the stress fields of Problem (a) and Problem (b), the same is not true for elastic energies. By the way, the elastic energy of Problem (b) has a positive value and can be expressed as

$$E_{\text{el}}^{(b)} = \frac{1}{2} \int_{\partial\Omega} \mathbf{T}^{\text{img}} \cdot \mathbf{u}^{\text{img}} dS = -\frac{1}{2} \int_{\partial\Omega} \mathbf{T}^{\infty} \cdot \mathbf{u}^{\text{img}} dS \quad (\text{C.2})$$

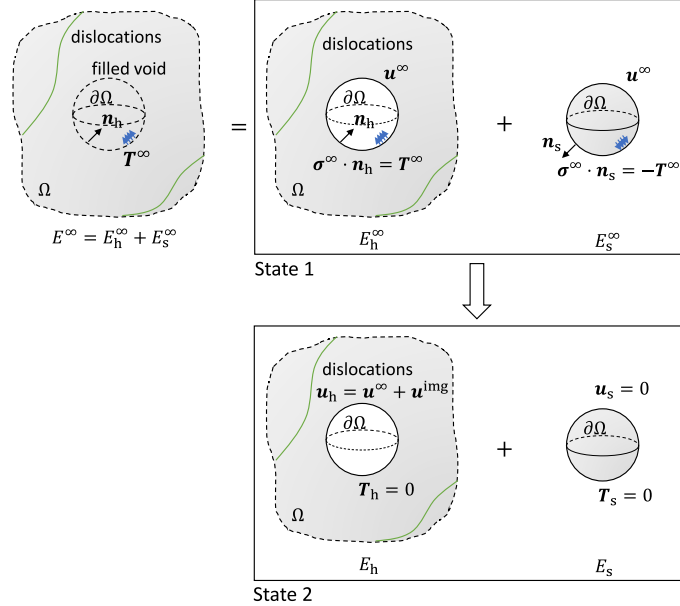


Figure C.6: A reversible path between two states. In State 1, a spherical region is carved out of an infinite medium containing dislocations, but traction forces are applied to the surfaces of both the void and the sphere to maintain the stress field of dislocations in an infinite medium. In State 2, the traction forces on both surfaces have been removed.

To derive $E_{\text{el}}^{\text{img}}$, we consider a reversible path between two states shown in figure C.6, and $E_{\text{el}}^{\text{img}}$ is the work done to the elastic medium along this path. Starting from an infinite medium containing dislocations but no void,

State 1 is obtained by cutting the spherical region out of the medium but maintaining tractions on the surfaces of both the void and the solid sphere. The traction on the void surface is $\mathbf{T}^\infty = \boldsymbol{\sigma}^\infty \cdot \mathbf{n}_h$, where \mathbf{n}_h is the surface normal of the void (pointing towards the spherical center); the traction on the solid sphere surface is $-\mathbf{T}^\infty = \boldsymbol{\sigma}^\infty \cdot \mathbf{n}_s$, where \mathbf{n}_s is the surface normal of the sphere (pointing away from the spherical center). The elastic energy of State 1 is the same as E_{el}^∞ .

State 2 is obtained from State 1 by gradually reducing the magnitude of the tractions to zero, on both the hole and sphere surfaces. On the hole surface, since the traction goes from \mathbf{T}^∞ to 0 as the displacement increments by \mathbf{u}^{img} , the work done is,

$$\Delta W_h = \frac{1}{2} \int_{\partial\Omega} \mathbf{T}^\infty \cdot \mathbf{u}^{\text{img}} dS \quad (\text{C.3})$$

On the solid sphere surface, since the traction goes from $-\mathbf{T}^\infty$ to 0 as the displacement changes from \mathbf{u}^∞ to 0 (assuming no dislocations in the sphere), the work done is,

$$\Delta W_s = \frac{1}{2} \int_{\partial\Omega} (-\mathbf{T}^\infty) \cdot (-\mathbf{u}^\infty) dS = \frac{1}{2} \int_{\partial\Omega} \mathbf{T}^\infty \cdot \mathbf{u}^\infty dS \quad (\text{C.4})$$

Therefore,

$$E_{\text{el}}^{\text{img}} = \Delta W_h + \Delta W_s = \frac{1}{2} \int_{\partial\Omega} \mathbf{T}^\infty \cdot (\mathbf{u}^\infty + \mathbf{u}^{\text{img}}) dS \quad (\text{C.5})$$

which proves equation (6). The negative derivative of the image elastic energy $E_{\text{el}}^{\text{img}}$ with respect to the dislocation position gives the attractive force exerted by the void on the dislocation, which (for self-consistency) is identical to the Peach-Koehler force of the image stress, as demonstrated in Section 4.3.

Appendix D. Boundary value problems

In this section, we provide the definitions of the exact boundary value problems in figure 1. For isotropic homogeneous materials in the absence of body forces, the governing equation for the problem shown in figure 1(c) is:

$$\mu u_{j,kk} + (\lambda + \mu) u_{k,kj} = 0, \quad (\text{D.1})$$

where u_j is the displacement field, from which the stress field can be obtained as,

$$\sigma_{ij} = \lambda \delta_{ij} u_{k,k} + \mu (u_{i,jj} + u_{j,ij}). \quad (\text{D.2})$$

The boundary conditions over the traction-free surface can be written as,

$$T_j \equiv \sigma_{ij} n_j = 0, \quad \text{on } \partial\Omega. \quad (\text{D.3})$$

The stress field is generated by the presence of dislocations in the medium, i.e. the “source terms”. Formally, these source terms can be written in terms of a discontinuity condition on the displacement field (Hirth and Lothe, 1982),

$$\oint_C \frac{\partial u_j}{\partial l} dl = b_j \quad (\text{D.4})$$

where C is any closed path (i.e. the Burgers circuit) that encloses the dislocation line and b_j is the Burgers vector of the dislocation.

The boundary value problems in figure 1(a) and (b) satisfy the same PDE as in (c) but are subjected to different boundary conditions. Furthermore, the solutions in (c) is the superposition of the solutions in (a) and (b), and we use superscripts ^{tot}, [∞], ^{img} to designate the solutions in (c), (a), (b), respectively.

$$\begin{aligned} u_j^{\text{tot}} &= u_j^\infty + u_j^{\text{img}}, & \sigma_{ij}^{\text{tot}} &= \sigma_{ij}^\infty + \sigma_{ij}^{\text{img}}, & \text{in } \Omega \\ T_j^{\text{tot}} &= T_j^\infty + T_j^{\text{img}} = 0, & & \text{on } \partial\Omega \end{aligned} \quad (\text{D.5})$$

The problem in figure 1(a) corresponds to dislocations in an infinite medium. So the displacement field u_j^∞ satisfies the discontinuity condition, equation (D.4), which is the only boundary condition for problem (a). However, the traction field T_j^∞ evaluated on $\partial\Omega$ is generally non-zero. Because the stress field of a dislocation in an infinite isotropic medium is available analytically (Hirth and Lothe, 1982), T_j^∞ can be easily evaluated on $\partial\Omega$.

The problem in figure 1(b) corresponds to an elastic medium containing a spherical hole but no dislocations. So its displacement field u_j^{img} is continuous and no longer needs to satisfy the discontinuity condition, equation (D.4). The stress source for this problem is the traction boundary condition:

$$T_j^{\text{img}} = -T_j^\infty \quad \text{on } \partial\Omega. \quad (\text{D.6})$$

References

- [1] D. Ahn, P. Sofronis, R. Minich, On the micromechanics of void growth by prismatic-dislocation loop emission, *Journal of the Mechanics and Physics of Solids* 54 (2006) 735 – 755.
- [2] A. Arsenlis, W. Cai, M. Tang, M. Rhee, T. Opperstrup, G. Hommes, T. G. Pierce, V. V. Bulatov, Enabling strain hardening simulations with dislocation dynamics, *Modelling and Simulation in Materials Science and Engineering* 15 (2007) 553.
- [3] J. R. Barber, *Elasticity*, volume 172, Springer Science & Business Media, 2009.
- [4] R. G. Barrera, G. A. Estevez, J. Giraldo, Vector spherical harmonics and their application to magnetostatics, *European Journal of Physics* 6 (1985) 287.
- [5] A. A. Benzerga, J.-B. Leblond, A. Needleman, V. Tvergaard, Ductile failure modeling, *International Journal of Fracture* 201 (2016) 29–80.
- [6] W. Cai, A. Arsenlis, C. R. Weinberger, V. V. Bulatov, A non-singular continuum theory of dislocations, *Journal of the Mechanics and Physics of Solids* 54 (2006) 561 – 587.
- [7] H.-J. Chang, J. Segurado, J. LLorca, Three-dimensional dislocation dynamics analysis of size effects on void growth, *Scripta Materialia* 95 (2015) 11 – 14.
- [8] S. Gavazza, D. Barnett, The elastic interaction between a screw dislocation and a spherical inclusion, *International Journal of Engineering Science* 12 (1974) 1025 – 1043.
- [9] E. van der Giessen, A. Needleman, Discrete dislocation plasticity: a simple planar model, *Modelling and Simulation in Materials Science and Engineering* 3 (1995) 689.
- [10] J. P. Hirth, J. Lothe, *Theory of Dislocations*, Krieger Publishing Company, 2nd edition, 1982.
- [11] E. W. Hobson, *The theory of spherical and ellipsoidal harmonics*, Cambridge University Press, 1931.

- [12] R. A. Lebensohn, J. P. Escobedo, E. K. Cerreta, D. Dennis-Koller, C. A. Bronkhorst, J. F. Bingert, Modeling void growth in polycrystalline materials, *Acta Materialia* 61 (2013) 6918 – 6932.
- [13] V. Lubarda, M. Schneider, D. Kalantar, B. Remington, M. Meyers, Void growth by dislocation emission, *Acta Materialia* 52 (2004) 1397 – 1408.
- [14] A. Misra, M. J. Demkowicz, X. Zhang, R. G. Hoagland, The radiation damage tolerance of ultra-high strength nanolayered composites, *JOM* 59 (2007) 62–65.
- [15] L. B. Munday, J. C. Crone, J. Knap, The role of free surfaces on the formation of prismatic dislocation loops, *Scripta Materialia* 103 (2015) 65 – 68.
- [16] G. Potirniche, J. Hearndon, M. Horstemeyer, X. Ling, Lattice orientation effects on void growth and coalescence in fcc single crystals, *International Journal of Plasticity* 22 (2006) 921 – 942.
- [17] G. Potirniche, M. Horstemeyer, G. Wagner, P. Gullett, A molecular dynamics study of void growth and coalescence in single crystal nickel, *International Journal of Plasticity* 22 (2006) 257 – 278.
- [18] M. H. Sadd, Chapter 13 - displacement potentials and stress functions: Applications to three-dimensional problems, in: M. H. Sadd (Ed.), *Elasticity (Third Edition)*, Academic Press, Boston, third edition edition, 2014, pp. 397 – 421.
- [19] H. R. Sadraie, S. L. Crouch, S. G. Mogilevskaya, A boundary spectral method for elastostatic problems with multiple spherical cavities and inclusions, *Engineering Analysis with Boundary Elements* 31 (2007) 425 – 442. *Innovative Numerical Methods for Micro and Nano Mechanics and Structures - Part I*.
- [20] J. Segurado, J. LLorca, Discrete dislocation dynamics analysis of the effect of lattice orientation on void growth in single crystals, *International Journal of Plasticity* 26 (2010) 806 – 819.
- [21] J. Segurado, J. Llorca, An analysis of the size effect on void growth in single crystals using discrete dislocation dynamics, *Acta Materialia* 57 (2009) 1427 – 1436.

- [22] R. B. Sills, W. P. Kuykendall, A. Aghaei, W. Cai, *Fundamentals of Dislocation Dynamics Simulations*, Springer International Publishing, Cham, pp. 53–87.
- [23] D. R. Steinmetz, T. Jpel, B. Wietbrock, P. Eisenlohr, I. Gutierrez-Urrutia, A. SaeedAkbari, T. Hickel, F. Roters, D. Raabe, Revealing the strain-hardening behavior of twinning-induced plasticity steels: Theory, simulations, experiments, *Acta Materialia* 61 (2013) 494 – 510.
- [24] S. Traiviratana, E. M. Bringa, D. J. Benson, M. A. Meyers, Void growth in metals: Atomistic calculations, *Acta Materialia* 56 (2008) 3874 – 3886.
- [25] V. Tvergaard, Material failure by void growth to coalescence, *Advances in Applied Mechanics* 27 (1989) 83 – 151.
- [26] D. A. Varshalovich, A. N. Moskalev, V. K. Khersonskii, *Clebsch-Gordan coefficients and 3jm symbols*, World Scientific, pp. 235–289.
- [27] C. R. Weinberger, W. Cai, Computing image stress in an elastic cylinder, *Journal of the Mechanics and Physics of Solids* 55 (2007) 2027 – 2054.
- [28] M. Wiecek, M. Meschede, E. S. de Andrade, I. Oshchepkov, *Shtools: Version 4.0*, 2016.
- [29] J. R. Willis, R. Bullough, The interaction between a void and a dislocation loop, in: *voids formed by irradiation of reactor materials*, The British Nuclear Energy Society, 1969, pp. 133–147.
- [30] J. R. Willis, M. R. Hayns, R. Bullough, The dislocation void interaction, *Proceedings of the Royal Society of London A: Mathematical, Physical and Engineering Sciences* 329 (1972) 121–136.